RESEARCH Open Access

Transition front prediction for the HyTRV model based on multi-dimensional stability theories

Ligeng Zhang[1], Xi Chen[1*], Shuyi Liu[1], Qian Wang[1], Siwei Dong[1], Maochang Duan[1] and Jianqiang Chen[1*]

[1] State Key Laboratory of Aerodynamics, Mianyang 621000, China

Abstract

The prediction of three-dimensional boundary layer transition has long been an important issue in aircraft design. The eN method based on one-dimensional stability theories (LST-eN) is widely used in transition prediction, yet fails to capture transition features of large-scale vortical structures commonly present on the vehicle surface. The vortical structures cause substantial spanwise variations of the base flow and thereby render the one-dimensional stability theories invalid. We in the present study modulate the eN method by exploiting multi-dimensional stability theories, especially the plane-marching parabolized stability equations (PSE3D), to predict the windward transition front of a lifting body under a high-speed flight condition (FLT) and a wind-tunnel condition with two angles of attack (WT1 with 2-degree angle of attack and WT2 with 4-degree angle of attack). The modal instability characteristics for the centerline vortex region in these three cases are similar, featuring the upstream Mack-mode instability and the downstream vortex instabilities. The transition *N*-factor front qualitatively aligns well with direct numerical simulation (DNS) results for the flight case and the experimental measurements for the wind-tunnel cases. The transition *N*-factor is correlated to be around 2 for the flight case (based on the DNS data), around 4 for the wind-tunnel case WT1 and around 2 for the wind-tunnel case WT2. Intriguingly, the WT2 case experiences an earlier transition than the WT1 case although the former turns out to be more stable as predicted by the modal stability analysis. Preliminary non-modal analysis shows that non-modal growth is stronger in the WT2 case than in the WT1 case, implying that non-modal disturbances may play a role in the transition process. The cross-flow instability is also addressed for the flight case, focusing on the comparison of results from the one- and multi-dimensional stability analyses.

Keywords: Boundary-layer transition, Streamwise vortices, Global stability analysis, Non-modal analysis

1 Introduction

Boundary layer transition exhibits a significant impact on the heat flux and friction coefficient on the surface of high-speed vehicles, making accurate transition prediction crucial for the designers [1]. The eN method, assuming that transition occurs when the

integrated amplification (N-factor) of disturbances exceeds some threshold value, is one of the most commonly used ways to predict transition location [2–4].

The traditional eN method is based on the one-dimensional linear stability theory (LST) [5] and/or parabolized stability equations (PSE) [6], and is abbreviated as the LST-eN method hereafter for brevity. The N-factor prediction is usually associated with the stability investigation of the actual flight vehicles such as the HIFiRE-1 conical model, the HIFiRE-5 elliptical conical model, and the BoLT model. Alba et al. [7] conducted a comparison between the N-factors obtained by PSE analysis and the experimental as well as computational outcomes on the HIFiRE-1 model. At 0° angle of attack, the predicted N-factor for the transition is approximately 5.5, whereas the prediction for non-zero attack angles was unsuccessful. Li et al. [8] employed the PSE to analyze the HIFiRE-1 and HIFiRE-5 geometry and acquired a second-mode transition N-factor of approximately 13.5, and attained a peak frequency that was in correspondence with the experimental results on the HIFiRE-5 geometry. Lakebrink et al. [9] utilized LST, LPSE, and 2pLPSE to analyze the stationary and traveling cross-flow instabilities on the HIFiRE-5 geometry and achieved good agreement with the wind tunnel experimental results through the latter two methods. The transition N-factor was around 8. Moyes et al. [10] and Tufts et al. [11] adopted LPSE to analyze the flow field on the HIFiRE-5b geometry and compared the results with flight test data, discovering that the second-mode transition N-factor near the attachment-line ranges between 16 and 18, and the transition N-factor for the steady cross-flow vortices is 10. Berridge et al. [12] carried out wind tunnel experiments and LST analyses on the BoLT geometry and determined that the corresponding N-factor for the second-mode transition in the noisy environment was 3.1, while the peak frequency in LST analysis mismatches with the experiment. Moyes et al. [13, 14] utilized LPSE and NPSE to analyze the cross-flow transition on the BolT geometry and obtained good consistency with the wind tunnel experiment. They further pointed out that the interaction between the steady and traveling cross-flow waves is the cause of the disparity between the quiet wind tunnel experiment and the NPSE for the HIFiRE-5 study. Simultaneously, NPSE is efficient in capturing the streak distribution. Currently, the LST-eN method has been successful in predicting the cross-flow transitions, with the critical N-factor distributed around 8 to 10.

Nevertheless, issues remain to be addressed. A complicated vortex system usually appears over the vehicle during the cruise, such as the HIFiRE-5 or BoLT. These vortices distort the mean flow and give rise to highly inflectional profiles not only in the wall-normal direction but also in the spanwise direction, thereby introducing new instabilities to the flow field. However, one-dimensional methods ignore the spanwise inhomogeneity of base flows, rendering them inefficient to apply in such flow fields. What's more, it requires a priori knowledge of the disturbance propagation path, together with the variation of the span-wise wavelength along this path, to track the downstream development of disturbances [15, 16]. These inherent drawbacks of one-dimensional theories constrain their applications, highlighting the significance of developing three-dimensional prediction analysis tools.

Different from LST-eN method, multi-dimensional stability theories, named as global theories hereafter, take the spanwise variations of the base flow into account, and avoid specifying the integration path of disturbances. The global method has been successfully

applied to investigate the stability of streamwise vortices of three-dimensional boundary layers [17, 18]. Of particular interest is the transition N-factor of the vortices. Based on the transition locations in DNS where transition was triggered by random blowing and suction, Chen et al. [19] established the transition N-factor to be approximately 10 for the vortex over a yawed cone, while the transition N-factor can be even below 2 for a similar configuration in conventional wind tunnels [20–22]. On the other hand, Choudhari et al. [23] obtained a transition N-factor of 15 on the HIFiRE-5 model based on flight experiments. Moreover, several studies obtained the N-factor distribution based on the global approaches [24, 25], although no further comparison to the experiment nor DNS was provided. Recently, Araya et al. [26, 27] employed a series of stability analysis tools to investigate the stability of vortices on a finned cone under a wind-tunnel condition and presented the N-factor front of the dominant frequency, which exhibits a strong correlation with the measured heat flux distribution in wind-tunnel experiments. The transition N-factor corresponding to the saturation location of the wall pressure disturbances measured in experiments is around 3–5. The discrepancy of the transition N-factors among different studies likely stems from differences in the disturbance level, the model configurations, the wall-temperature ratio, or even the transition mechanisms, and warrants further investigation to clarify the key factors.

Therefore, the primary objective of this paper is to analyze the linear stability characteristics of the flow field on the same vehicle model under a variety of conditions, namely one flight condition and two wind-tunnel conditions using multi-dimensional stability theories (BiGlobal and PSE3D), and try to calibrate the transition N-factors based on the experiment and numerical data. The vehicle model we adopted is the so-called lifting body HyTRV model which was shown to be able to support multiple instabilities [28–31]. We will, for the first time to our knowledge, reveal the vortex instability characteristics (and the crossflow instability characteristics for the flight case), and predict the pertaining transition front over the HyTRV model. The content of this paper is organized as follows: Section 2 presents the basic flow calculation settings and introduces the global linear stability method and the optimal growth method; Section 3 displays the stability analysis results along with transition fronts of the flight and wind-tunnel conditions, together with the DNS and optimal analysis results. A comparison to the LST-eN method is made during the analysis of the cross-flow under the flight condition; lastly, Section 4 concludes with a summary.

2 Computational settings and analysis methods

2.1 Base flow computation

The HyTRV model utilized in the present study is illustrated in Fig. 1. Two coordinate systems are involved, namely, the Cartesian coordinate (X, Y, Z) denoting streamwise, wall-normal, and spanwise coordinates, respectively, with corresponding velocities (u, v, w) and the local body-fitted coordinate (ξ, η, ζ) with corresponding velocities (u_n, v_n, w_n). The asterisk in this paper denotes the dimensional form, and variables without an asterisk refer to nondimensional form. Three conditions are investigated in this paper, namely one flight condition (FLT) and two wind tunnel conditions (WT1 and WT2). The wall temperature ratio (the ratio of the wall temperature to the adiabatic wall temperature) of the flight case is 0.3, which is lower than that of

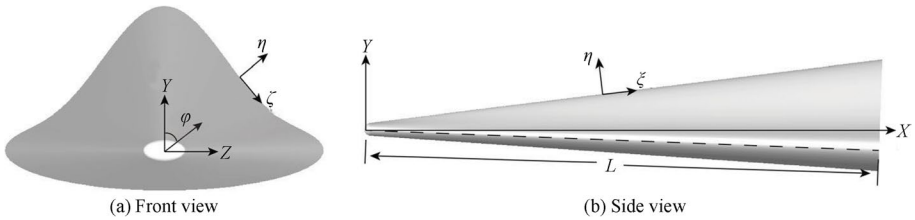

Fig. 1 The model geometry and Cartesian/body-oriented coordinates used in the present study. $L^* = 1600$ mm for the flight case and $L^* = 400$ mm for the wind-tunnel cases

Table 1 The base flow parameters that are used for the stability analysis

	$Re_\infty\ (m^{-1})$	*Ma*	Farfield temp. T_e (K)	Wall temp. T_w (K)	AoA (°)	Model scale
FLT	1.7×10^7	6	216	500	2	1
WT1	2.0×10^7	6	79	300	2	0.25
WT2	2.0×10^7	6	79	300	4	0.25

the wind tunnel cases (0.7). The only difference between the two wind tunnel conditions is the angle of attack. The parameter settings for the three cases considered in this paper are summarized in Table 1. The wind-tunnel experiment adopts a 1:4 scale HyTRV model relative to the flight test. The parallel computational fluid dynamics software OPENCFD [32] is utilized for calculating the base flow. The calculation is divided into two sequential steps. In the first step, a second-order finite-volume scheme is employed to calculate the steady laminar flow over the entire model. Subsequently, this calculated flow field serves as both the inlet and outflow conditions for the refined calculation with high-order finite-difference schemes performed in a smaller near-wall region downstream of the nose. In this second step, a grid configuration consisting of 520 nodes in the streamwise direction, 741 nodes in the azimuthal direction, and 241 nodes in the wall-normal direction is adopted. Compared with the previous DNS (direct numerical simulation) study on a similar configuration [31, 33], the base flow can be adequately resolved under this grid resolution. The grid information was stated in detail by Ref. [31].

2.2 Transition profile acquisition

For the flight condition, we obtain the transition profile through direct numerical simulation. The computation is based on the truncated flow field acquired in the second step of the basic flow calculation, and the grid is symmetrically expanded and refined in the windward area to resolve the vortex breakdown, with a slight compromise on the spanwise resolution in the leeward and cross-flow regions. The grid possesses 1200× 1500×300 points in the streamwise, spanwise, and wall-normal directions. Here, the viscous terms are discretized using an 8th-order central difference scheme and the inviscid terms are discretized by a high-order mixed scheme. A random blowing and suction with an amplitude of $0.01U_e$ is applied to the upstream surface to ensure the transition.

The transition situation for wind-tunnel conditions is obtained by the previous experiments conducted by Liu et al. [30] in conventional wind tunnels. The surface heat flux is visualized by the infrared thermal imaging technology.

2.3 Modal stability theories

In the context of two-dimensional stability theory, the flow field can be decomposed into a base flow and an infinitesimal disturbance component. With body-fitted coordinates (ξ, η, ζ) representing streamwise, wall-normal, and spanwise directions, the decomposition is written as

$$\boldsymbol{q}(\xi, \eta, \zeta, t) = \bar{\boldsymbol{q}}(\eta, \zeta) + \varepsilon \hat{\boldsymbol{q}}(\eta, \zeta) \exp(i\alpha\xi - i\omega t) + c.c., \tag{1}$$

where $\varepsilon \ll 1$, α, ω, and *c.c.* represent the streamwise wave number, angular frequency, and complex conjugates, respectively. Notice that this decomposition employs the parallel flow assumption, i.e., ignoring the streamwise variation of the mean component $\bar{\boldsymbol{q}}$ and the disturbance shape function $\hat{\boldsymbol{q}}$. Under the spatial framework, α is a complex number and its imaginary part can be regarded as the amplification rate of the disturbance. After substituting the equation above into the N-S equations and neglecting nonlinear terms, we obtain a two-dimensional eigenvalue problem that is detailed in Chen et al. [31] (BiGlobal analysis) as

$$(\alpha^2 \mathcal{A} + \alpha \mathcal{B} + \mathcal{C})\hat{\boldsymbol{q}} = 0, \tag{2}$$

where $\mathcal{A}$, $\mathcal{B}$ and $\mathcal{C}$ are linear operators. No-slip and isothermal boundary conditions are imposed at the wall. For the symmetry plane (the centerline plane), either symmetric or antisymmetric boundary conditions are applied [18]. The disturbance is considered to be diminished at the far field. The eigenvalue is then obtained through the Arnoldi method [17]. After obtaining an unstable mode, the Newton-Raphson method [13] is then utilized to seek other unstable modes of the same family along the frequency and/or the axial direction.

The streamwise evolution of a single mode with fixed frequency can be accurately obtained by the PSE3D method, which considers the streamwise non-parallelism of the flow field. In the PSE3D formulation, the flow field is decomposed as

$$\boldsymbol{q}(\xi, \eta, \zeta, t) = \bar{\boldsymbol{q}}(\xi, \eta, \zeta) + \varepsilon \hat{\boldsymbol{q}}(\xi, \eta, \zeta) \exp(i \int_{\xi'} \alpha \mathrm{d}\xi' - i\omega t) + c.c., \tag{3}$$

which yields the parabolized stability equations by neglecting the second-order derivative of $\hat{\boldsymbol{q}}$ with respect to ξ as

$$\mathcal{L}\hat{\boldsymbol{q}} + \mathcal{M}\frac{\partial \hat{\boldsymbol{q}}}{\partial \xi} = 0, \tag{4}$$

where $\mathcal{L}$ and $\mathcal{M}$ are linear operaters. The parabolized equations are then solved by marching downstream from the inlet profiles provided by the BiGlobal analysis. Detailed information about the PSE3D method and the code verification can be referred to Ref. [34].

In this study, we utilize the eN method based on PSE3D to characterize the transition front. The N-factor is calculated as the natural logarithm of the ratio of the local perturbation magnitude to the initial amplitude. The transition front is then illustrated by the envelope of the isolines of the N-factor of every possible mode as

$$N_\phi(\xi,\zeta) = \text{maximum}\left[\ln\left(\frac{\phi(\xi,\zeta)\exp\left(\int_{\xi_0}^{\xi} -\alpha_i \mathrm{d}\xi'\right)}{\phi_{\max}(\xi_0)}\right)\right], \tag{5}$$

where ϕ represents the shape function magnitude of any one of the primary variables. ξ_0 is the neutral location where the mode begins to amplify. Upon the completion of the present study, we came across the recently published work by Araya et al. [27], who has also proposed a similar N-factor formulation based on the wall pressure amplitude. In the present study, however, we adopted the temperature component $\hat{T}$ to calculate N-factors, because the temperature component has generally the largest amplitude (several orders higher than the wall pressure) and thus likely more faithfully reflects the disturbance amplitude. The transition front is ultimately visualized by superimposing the PSE3D analysis results, assuming that the modes have the same initial amplitude at the neutral locations.

2.4 Optimal growth theory

As will be shown later, the results from the aforementioned modal analyses are not all in agreement with the experimental observations. Therefore, it is helpful to perform non-modal or optimal growth analysis to fill the gap between the modal stability analysis and the experimental results. In this subsection, we explain the methodology for the optimal growth analysis. Unlike the exponential growth of modal instability, the perturbation can have a transient algebraic growth in a short time as a result of the non-normality of the linearized Navier-Stokes operator [35]. This allows the disturbance amplitude to reach a relatively large value even without modal instabilities. The optimal initial perturbation $\boldsymbol{q}_0$ is characterized as the initial condition at ξ_0 that maximizes the objective function G at ξ_1. Here, the objective function G is defined as a metric for the perturbation growth within the designated interval $[\xi_0, \xi_1]$,

$$G = \frac{E_{\xi_1}(\hat{\boldsymbol{q}}_1)}{E_{\xi_0}(\hat{\boldsymbol{q}}_0)}, \tag{6}$$

where the E_ξ denotes the energy norm of $\hat{\boldsymbol{q}}$ as

$$E_\xi(\hat{\boldsymbol{q}}) = \int_\eta \hat{\boldsymbol{q}}^H \boldsymbol{M}_E \hat{\boldsymbol{q}}\, \mathrm{d}\eta. \tag{7}$$

The $\boldsymbol{M}_E$ is the energy weight matrix that reads

$$\boldsymbol{M}_E = \text{diag}\left[\frac{\bar{T}}{\gamma\bar{\rho}M^2}, \bar{\rho}, \bar{\rho}, \bar{\rho}, \frac{\bar{\rho}}{\gamma(\gamma-1)\bar{T}M^2}\right], \tag{8}$$

and the superscript H denotes the conjugate transpose. The issue regarding the determination of the maximum of the function G gives rise to an optimality system [36]. The

optimal growth is solved by performing the direct-adjoint loop using the 2-D PSE framework along the centerline given a spanwise wavenumber β. The amplification of the optimal disturbance is also expressed by the logarithmic amplification ratio based on the total energy norm, which is defined as

$$N_E = \frac{1}{2}\ln\left[\frac{E_\xi(\hat{\boldsymbol{q}})}{E_{\xi_0}(\hat{\boldsymbol{q}}_0)}\right]. \tag{9}$$

In this paper, only the stationary disturbances are studied since they are generally the optimal disturbances that could experience the largest energy growth in most flows [37]. Detailed description of this methodology and the code verification can be found in our recent work [38].

3 Results

3.1 The flight case

The calculated basic flow field is depicted in Fig. 2. It can be observed that owing to the three-dimensional effect, prominent vortex structure emerges in the vicinity of the windward centerline region, with its size gradually increasing downstream. The intricate nature of this vortex structure distorts the local flow field, resulting in high shear layers at a considerable distance away from the surface. Such a vortex structure is supposed to sustain highly unstable shear-layer instabilities. Obviously, it is necessary to consider the spanwise variations of the base flow in the stability analysis. The spanwise variation of the base flow can be quantified as

$$A_{\tilde{u}}(\xi,\eta) = \frac{\max(\tilde{u}) - \min(\tilde{u})}{2},\ \tilde{u}(\xi,\eta) = u(\xi,\eta,\zeta) - u_{\text{mean},\zeta}(\xi,\eta), \tag{10}$$

where $\tilde{u}$ denotes the streamwise velocity perturbation, the expressions max() and min() signify the maximum and minimum values along the azimuthal direction, and $u_{\text{mean},\zeta}$

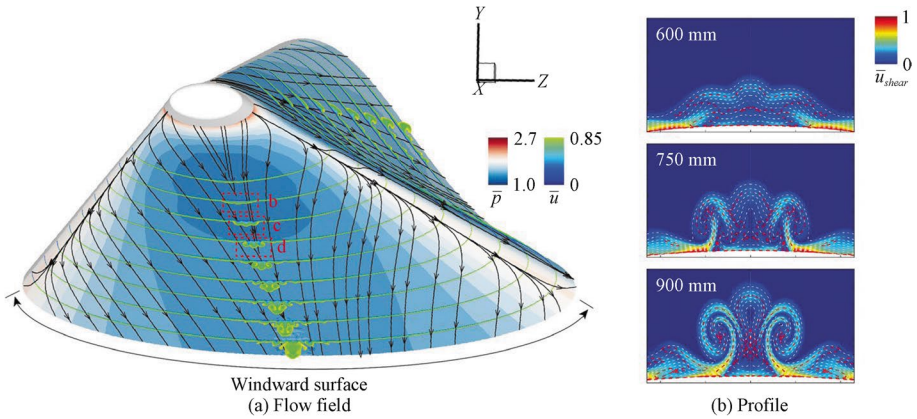

Fig. 2 **a** The base velocity $\bar{u}$ at different axial locations on the HyTRV model with surface streamlines. Zoom-in views of three representative stations near the windward centerline, namely **b** $X^* = 600$ mm, 750 mm, and 900 mm are also shown. The colored contours in **b** represent the normalized shear strength $(\bar{u}_y^2 + \bar{u}_z^2)^{1/2}$ of the flow field, with the red dashed lines indicating the general inflection points, namely, $(\rho\bar{u}_l)_l = 0$, of the flow field, where *l* represents the derivative along the direction of the velocity $\bar{u}$ gradient in the *Y*-*Z* plane, and the base velocity shown at $\bar{u} =$ [0.1:0.1:0.9] in white dashed lines

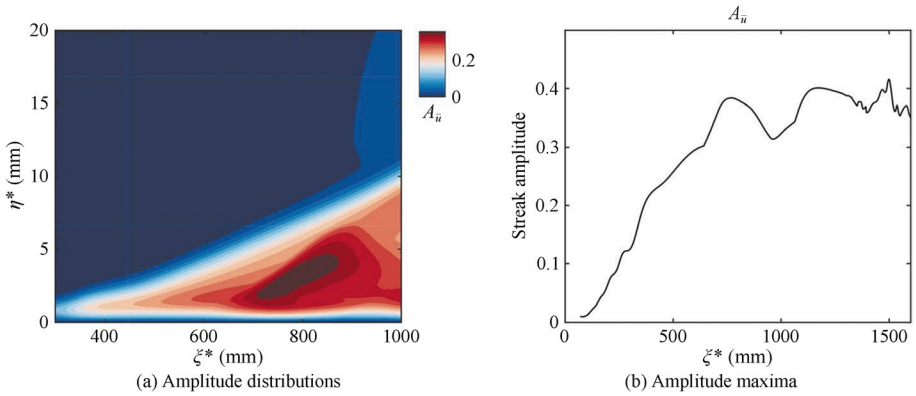

Fig. 3 **a** Spanwise variation of base flow, $A_{\bar{U}}$ along the streamwise and wall-normal directions. **b** The streak amplitude along the streamwise direction

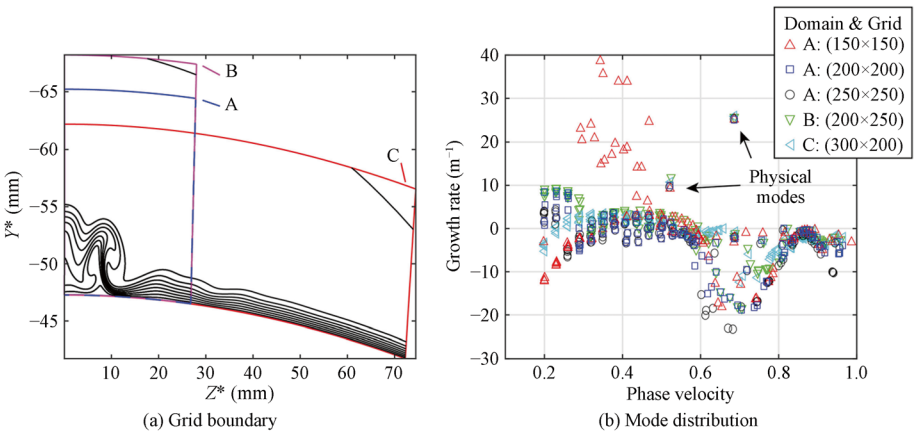

Fig. 4 **a** Three different computational domains and **b** the BiGlobal mode spectrum of 150 kHz at $X^* = 800$ mm. Domain A is utilized in the calculation, while domain B and domain C extend the boundary of domain A in the azimuthal direction and in the wall-normal direction, respectively

represents the average of the streamwise velocity at a certain ξ position in the ζ direction. The maximum in the wall-normal direction gives the streak amplitude [39, 40].

Figure 3 illustrates the variation of $A_{\bar{u}}$ along the streamwise and wall-normal directions. The upper edge of the streak rises continuously along the streamwise direction, with its maximum amplitude first appearing near the wall and lifting afterward. The streak amplitude continuously rises and reaches a peak around $X^* = 750$ mm, followed by a saturation stage.

Away from the centerline area, the fluid field features a cross-flow pattern where the fluid moves from the attachment line towards the centerline, and is thus susceptible to cross-flow instabilities. Below we will present stability analysis results for the vortex and cross-flow instabilities separately.

Before proceeding ahead, it is essential to verify the grid for the stability analysis. We separately assess the effects of the computational domain and the grid points as shown in Fig. 4. It can be clearly seen that the physical modes are already converged

for the baseline case (domain A with 150×150 points). The results hereafter are thus all obtained with the baseline case.

Figure 5 illustrates the modal characteristics within the centerline region from the BiGlobal method. It reveals three stages of mode instability characteristics ranging from $X^* = 300$ mm to 1000 mm. Mack modes [5] first become unstable and prevail at the first stage (300 mm $< X^* <$ 600 mm), featuring decreasing frequency downstream. Beyond about $X^* = 600$ mm, the streak instabilities manifest with two frequency peaks in the spectrum denoting the outer modes and inner modes, respectively [20, 41]. At this interval, the vortex instability at higher frequencies exhibits characteristics of a mixed Mack mode and outer mode, with the shape function residing between the wall surface and the relative sonic line, as well as at the inflection point. The inner modes dominate this second stage (600 mm $< X^* <$ 800 mm) and at about $X^* = 800$ mm are surpassed by the outer modes. The outer modes continuously expand into the higher-frequency region for $X^* >$ 800 mm (the third stage), which is consistent with the lift-up of the streaks shown in Fig. 3a.

Figure 6 shows the modal characteristics at one representative station for each stage. Firstly, in the upstream sections, the streamwise vortex has not yet formed, and only a low-speed region resembling the Klebanoff streak [42] is present in the flow field. At this stage, stability analysis identifies both planar and oblique Mack second mode instabilities. Notably, the maximum growth rate of the oblique Mack second mode is slightly larger than that of its planar counterpart, consistent with previous findings that streaks can suppress the planar second mode and promote the oblique ones with appropriate spanwise wave numbers [43, 44]. As the vortex evolves downstream, the Mack modes gradually morph into streak-instability modes as is also observed in previous studies [21, 45, 46]. The streak-instability modes can be further classified as outer modes with higher frequencies and phase velocities, and inner modes with lower frequencies and phase velocities [19]. The outer modes are located in the outer shear layers while the inner modes reside in the inner shear layers. The flow field at the third stage experiences a significant distortion, leading to an increase of unstable modes, as shown in Fig. 6e and f. It is worth mentioning that the antisymmetric

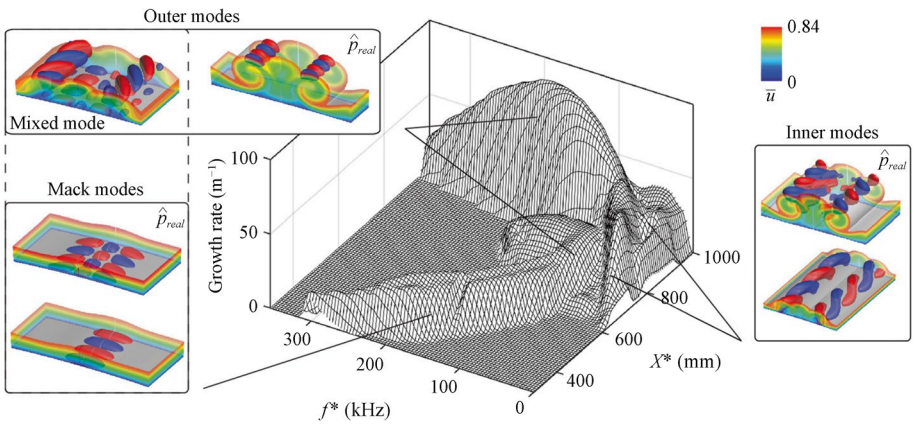

Fig. 5 The growth rate and frequency distribution of the most unstable modes in the centerline region from $X^* = 300$ mm to 1000 mm. The reconstructed real parts of the pressure shape functions are also shown

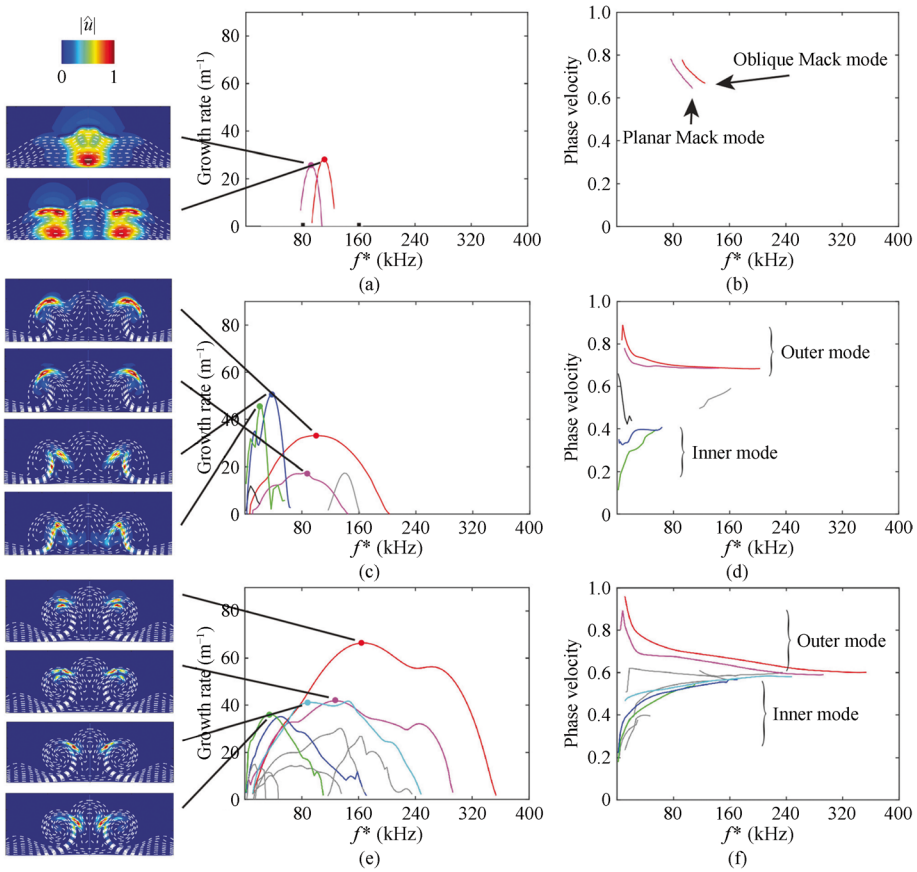

Fig. 6 The mode characteristic at three representative stations, namely **a**, **b** $X^* = 600$ mm, **c**, **d** $X^* = 800$ mm, and **e**, **f** $X^* = 975$ mm. The shape function $|\hat{u}|$ of the leading modes at each station is also shown

modes exhibit similar features as the symmetric counterpart, with generally smaller growth rates than the latter, and are thus not shown here.

The axial evolution of the N-factor associated with fixed-frequency disturbances is shown in Fig. 7a. The inlet conditions of PSE3D are the modal neutral points upstream obtained iteratively through BiGlobal analysis, namely the lower branch of planar and oblique Mack modes together with the neutral points of vortex modes, as depicted in Fig. 5. The frequency spans from 5 to 200 kHz. The modes in the frequency range around 100 to 120 kHz are the most amplified, of which the mode at 110 kHz can achieve the largest N-factor at the end of the model. The streamwise evolution of the modal shape function at 110 kHz is depicted in Fig. 7b, clearly showing how the upstream (oblique) Mack mode morphs into an outer mode and moves to the shoulder of the mushroom structure downstream.

Global stability analyses for the cross-flow instabilities are performed for the entire windward surface and the reduced method proposed by Chen et al. [31] is utilized to reduce the computation cost. Figure 8 illustrates the characteristics of cross-flow modes at a representative station $X^* = 750$ mm. The mode distribution falls within the frequency range of 0 kHz to 40 kHz, with the peak growth rate appearing at around 22 kHz. In comparison to streamwise vortex modes, the maximum growth

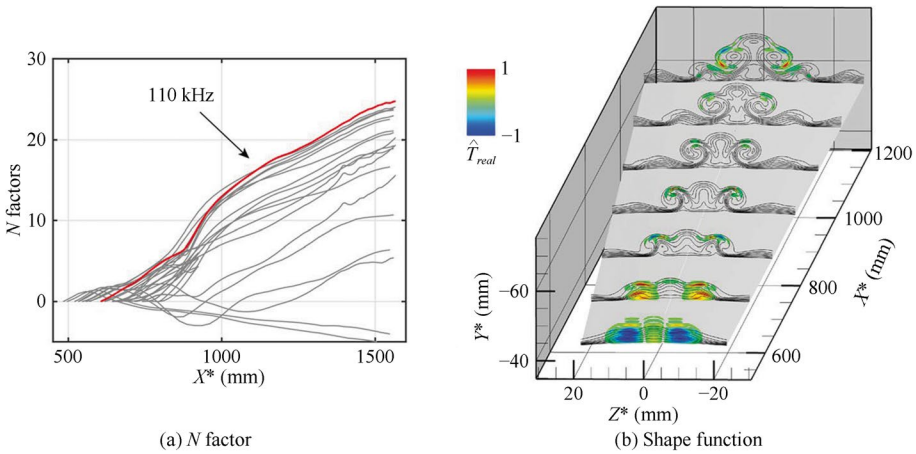

Fig. 7 **a** The *N*-factors obtained by PSE3D analysis, with the red line representing disturbance at 110 kHz. **b** The temperature shape function at several stations from $X^* = 500$ mm to 1200 mm for the 110 kHz case

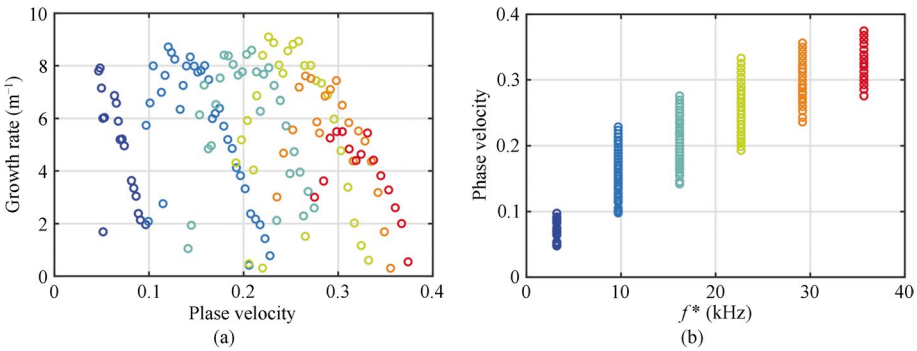

Fig. 8 The spectra of the cross-flow modes at $X^* = 750$ mm. The color represents frequency

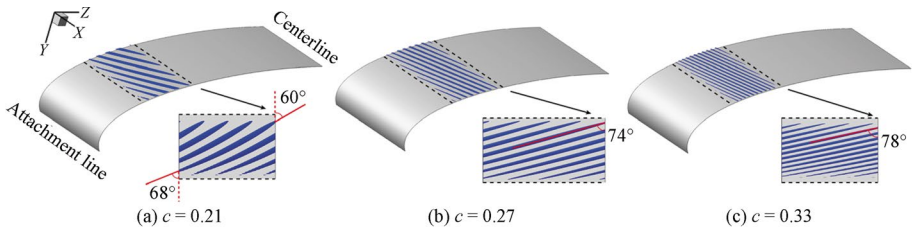

Fig. 9 The normalized real part of the temperature eigenfunction ($\hat{T} = 0.5$) for three modes with the same frequency 22 kHz in the cross-flow region: **a** $c = 0.21$, **b** $c = 0.27$, **c** $c = 0.33$. Four streamwise wavelengths of each mode are shown. The zoomed-in views of the main region of each shape function are also shown

rate of cross-flow mode is significantly lower. The spatial reconstruction of normalized shape functions of cross-flow modes with different phase velocities at 22 kHz is depicted in Fig. 9. It can be observed that the spanwise deflection angle of the shape function gradually increases with increasing phase velocity, while the azimuth location remains unchanged. For the mode with a lower phase velocity (Fig. 9a), the azimuth deflection angle near the attachment line is slightly larger than that near the

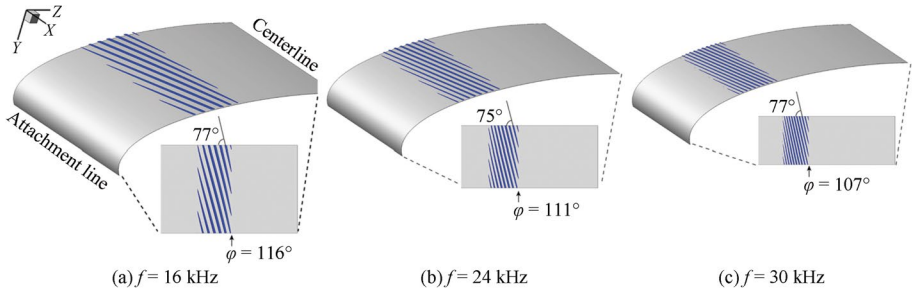

Fig. 10 The normalized real part of the temperature eigenfunction ($\hat{T} = 0.5$) for three modes with the same normalized phase velocity ($c/U_e = 0.24$) in the cross-flow region: **a** $f^* = 16$ kHz, **b** $f^* = 24$ kHz, **c** $f^* = 30$ kHz. Four streamwise wavelengths of each mode are shown. The projections on *X*-*Z* plane of each shape function are also shown

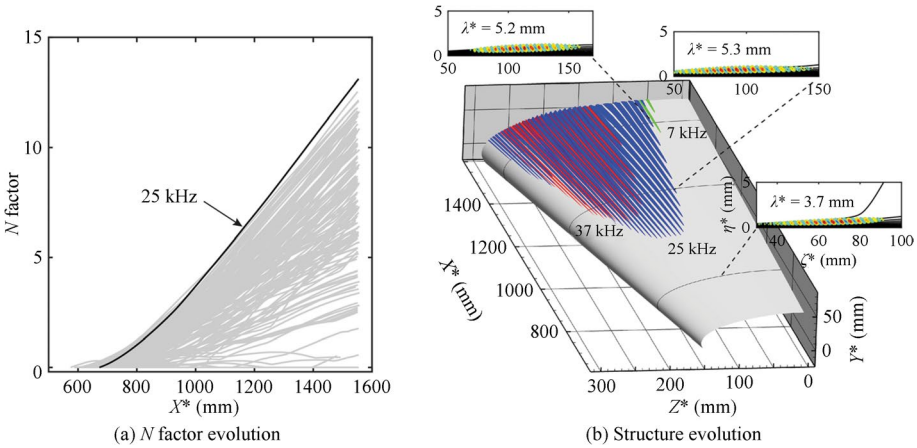

Fig. 11 **a** The evolution of the *N* factors for cross-flow modes obtained by PSE3D, together with the most amplified mode depicted by a bold black line. **b** The structure evolution, illustrated by the real part of the temperature disturbance with amplitude beyond 50 times the initial value at three representative frequencies, 7 kHz, 25 kHz and 37 kHz, together with enlarged images for 25 kHz showing mode shapes at selected stations and their corresponding azimuthal wavelength λ^*

centerline. The spatial reconstruction results of modal shape functions at different frequencies with nearly the same phase velocity are further compared in Fig. 10. It can be observed that as the frequency increases, the spanwise wavelength of the modes gradually decreases, and their distribution area shifts towards the shoulder attachment line. Furthermore, there is no significant variation in the spanwise deflection angle of the modal shape function with respect to frequency.

Next, we employed PSE3D to trace the downstream evolution of a series of nearly neutral modes at various frequencies. On account of the large number of cross-flow modes, only the nearly neutral ones at the upstream stations between $X^* = 600$ and 700 mm are chosen as the inlet conditions, with a frequency range from 4 to 40 kHz, amounting to a total of 180 cases, and approximately 20 modes per frequency. Figure 11a illustrates the diagram of modal *N*-factors calculated by PSE3D, wherein the mode with the largest *N*-factor near the end of the model is observed at 25 kHz. Figure 11b presents the real part of the temperature disturbance shape function beyond 50 times the initial value for dominant modes at different frequencies, and also provides zoomed-in images

from three specific locations for the most amplified one (25 kHz). It can be observed that there is no significant change in azimuthal location relative to the model during downstream evolution for each mode. Although different frequencies of the modes in the cross-flow region occupy separated azimuthal positions, as the disturbance amplitude increases beyond a certain threshold, there is an overlap between different disturbances, potentially leading to nonlinear effects. Furthermore, the local wavelength of the most amplified mode undergoes a gradual growth, starting with around 4 mm at the entrance, reaching approximately 5 mm near $X^* = 900$ mm and remaining at around 5–6 mm thereafter.

Figure 12 depicts the transition front of the streamwise vortex zone acquired through two approaches, namely LST-eN and PSE3D-eN. Although the BiGlobal analysis method is capable of obtaining the global modal characteristics of one certain station, it neglects the non-parallel effects that may introduce errors into the prediction [47]. More importantly, it is very difficult to accurately determine the local growth rate to be integrated when multiple unstable modes coexist since different modes may transform with each other. Therefore, PSE3D is used to trace downstream evolution of disturbances and thereby to obtain the *N*-factor. It can be observed that in contrast to the LST-eN method, PSE3D-eN exhibits significant superiority in the streamwise vortex zone. It should be noted that in the LST-eN method, a large *N*-factor front commences to emerge near $X^* = 800$ mm, which is due to the instability of the attachment line. Additionally, the cross-flow instability *N*-factor provided by the LST-eN method is larger, which might result from the distinct definitions of the *N*-factor: the *N*-factor in LST characterizes the

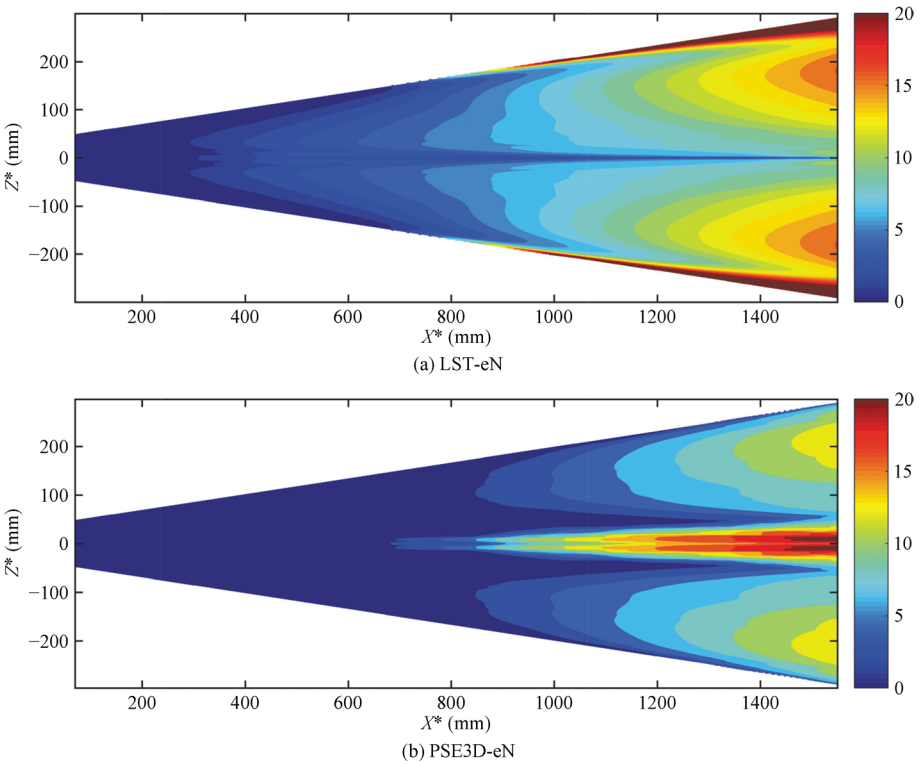

Fig. 12 *N*-factor front distribution obtained from **a** LST-eN and **b** PSE3D-eN methods

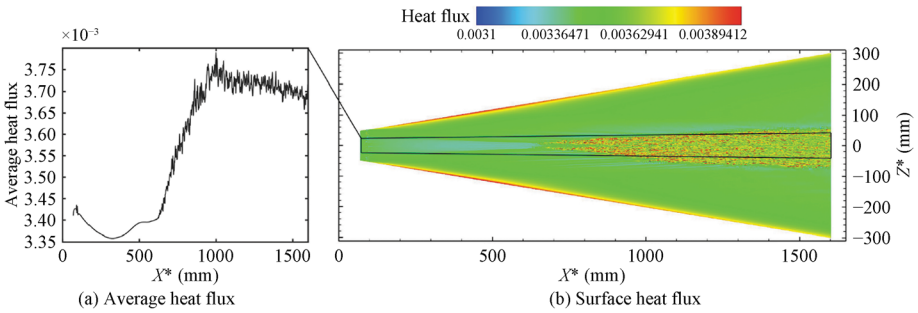

Fig. 13 The heat flux distribution of the HyTRV windward surface under the flight condition in DNS. Subplot **a** presents the distribution of the average heat flux within the black box marked in subplot **b** along the *X* direction

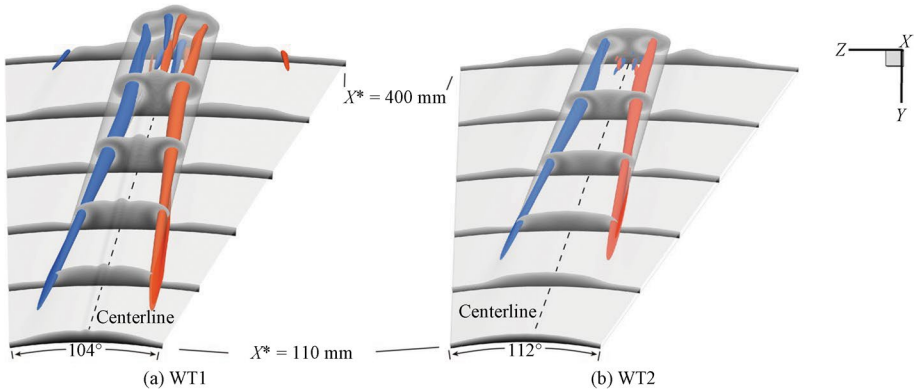

Fig. 14 The streamwise velocity and the *Q* criterion ($Q = 0.0004$, colored by the streamwise vorticity) isosurface of **a** case WT1 (2° AoA) and **b** WT2 (4° AoA)

amplitude amplification rate of the disturbance amplitude along a specific object surface line, while the *N*-factor in PSE3D considers the total energy growth of the disturbance from the global perspective.

Figure 13 depicts the instantaneous heat flux distribution obtained through direct numerical simulation. Transition occurs in the streamwise vortex region, yet no transition is witnessed in the cross-flow region, in accord with the aforementioned analysis results that the streamwise vortex instabilities are significantly more unstable than the cross-flow instabilities. Notably, two symmetrical transition fronts appear in the vicinity of the center line. The averaged heat flux reveals that the transition initiates around $X^* = 625$ mm. Clearly, the DNS transition front closely resembles the prediction by PSE3D (as shown in Fig. 12b), thus confirming the accuracy of the PSE3D method.

3.2 The wind-tunnel cases

In this subsection, we focus on the instability characteristics in the centerline region. Figure 14 depicts the streamwise velocity and *Q* criterion isosurface on the windward surface at 2° and 4° attack angles under wind-tunnel conditions. Similar to the flight condition, a low-velocity streak forms near the centerline due to the cross-flow convergence. Furthermore, an increase in attack angle delays the formation of outward vortex,

resulting in lower vortex height for the WT2 case. The elongated vortex tubes gradually approach the centerline downstream through vortex induction.

Figure 15a and b presents the contours of the locally largest growth rate of modal instabilities in the centerline region for cases WT1 and WT2, respectively. One observes that the instabilities under wind-tunnel conditions bear a strong resemblance to those in the flight condition, with apparent Mack modes appearing upstream followed by intrinsic streamwise vortex modes. To facilitate comparison of results from the flight and wind-tunnel cases, the neutral curves of three cases are displayed with respect to the relative length (X^*/L^*) in Fig. 15c. For case FLT and case WT1 at the same AoA, the Mack mode instabilities shear an overlap frequency range at the same relative positions of the model. However, there is a slight delay in the onset location of Mack mode in the wind-tunnel case compared to the flight case. We note that such a difference of Mack mode instabilities in these two cases is influenced by two competing effects. First, the cold-wall condition ($T_w/T_0 = 0.28$) of the flight case tends to enhance the Mack mode instability. Second, the bluntness Reynolds number of the flight case is significantly larger than that of the WT1 (the latter freestream Reynolds number should be four times the former one to reach the same bluntness Reynolds number), which may stabilize the Mack mode instability as is well known for two-dimensional configurations. Additionally, as depicted in Fig. 15b, oblique Mack mode is insignificant compared to its planar counterpart under the wind-tunnel condition while it is opposite under the flight condition (refer to Fig. 6a. This difference can be attributed to the distinct development of streak structures in each case's vortex region. In terms of vortex modes, outer modes are more unstable than inner modes for the wind-tunnel case throughout the entire model, whereas inner modes initially dominate at the onset of intrinsic vortex instabilities in the flight case.

Figure 15 also tells us how the AoA affects the modal stability of the vortex region. It shows that the onset of instabilities is markedly delayed as the AoA increases from 2° to 4°, which is consistent with the delay of the vortex formation (refer to Fig. 14). Consequently, the outer modes, which are most unstable, are stabilized, whereas the intrinsic low-frequency inner modes and Mack mode are slightly enhanced with increasing AoA, as is evident from Fig. 16.

Modal evolution obtained from PSE3D analyses is depicted in Fig. 17. The same strategy was employed as that utilized in the calculations of flight conditions. The

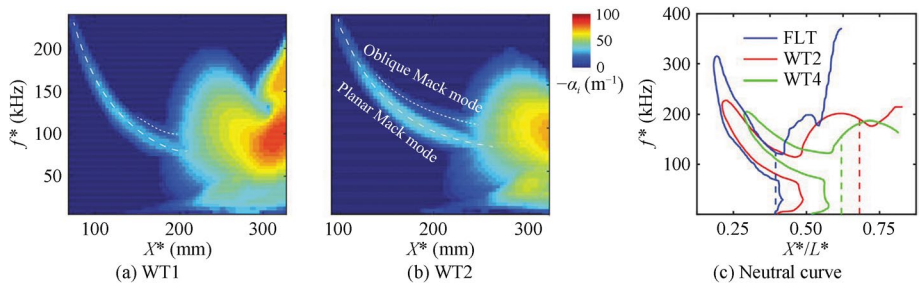

Fig. 15 The growth rate and frequency distribution of the most unstable modes in the centerline region for **a** case WT1 and **b** case WT2. The dashed and dotted lines in **a** and **b** are indications of peak frequencies of planar and oblique Mack modes, respectively. The **c** neutral curve of the studied cases are also shown, where streamwise locations are unified by the relative model length. The dashed lines in subfigure **c** indicate the transition locations measured in experiments and direct numerical simulation

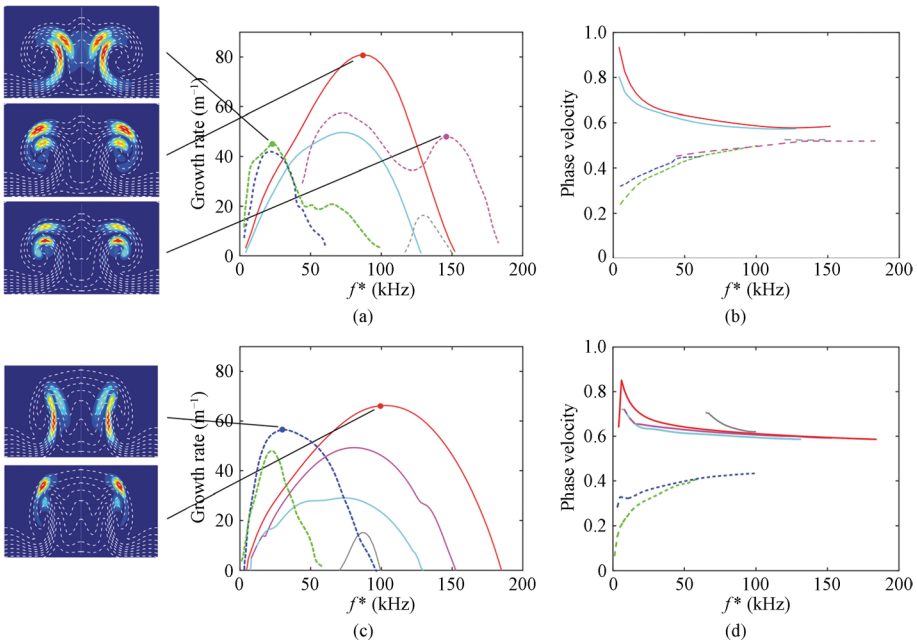

Fig. 16 Modal instability characteristics of **a**, **b** case WT1 (2° AoA) and **c**, **d** case WT2 (4° AoA) at $X^* = 300$ mm together with the shape function $|\hat{u}|$ of the leading modes. The dotted and solid lines represent inner and outer modes respectively

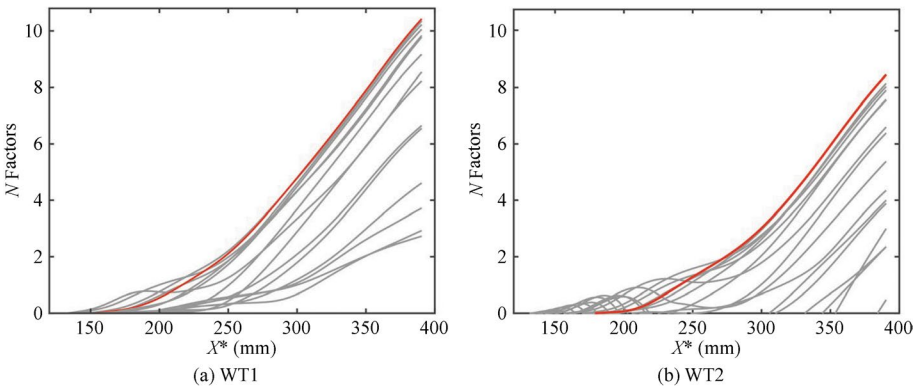

Fig. 17 The *N*-factors obtained by PSE3D analysis for **a** WT1 (2° AoA) and **b** WT2 (4° AoA) cases, with the red line representing disturbance at 96 kHz

oblique Mack modes are nearly neutral in wind tunnel conditions, so they were not taken into account in the PSE3D computations. Similar to the flight case, the Mack modes in the wind-tunnel cases are able to develop into vortex instability modes downstream. The most amplified disturbances at the end of the model are both initiated by planar Mack modes at around 96 kHz, as opposed to the flight case where the oblique Mack mode at around 110 kHz is the most dangerous. Albeit with commensurate peak growth rates, the corresponding *N*-factors (about 10 for case WT1 and 8.5 for case WT2) in the wind-tunnel cases are significantly smaller than that in the flight case (around 25), due to the scale difference.

We then draw a comparison of the *N*-factor distribution predicted by PSE3D and the heat-flux distribution obtained by wind-tunnel experiments, as shown in Fig. 18. In the WT1 case, it is observed that the transition *N*-factor is approximately 4. The heat-flux front emerges on both sides of the centerline, indicating that vortex mode instabilities may ultimately cause the transition. By contrast, a single heat-flux peak is experimentally observed at the centerline in case WT2, with a notably low *N*-factor of less than 2. This suggests that modal instability in the vortex region may not be the primary cause of transition. Similar findings have been reported in other studies conducted under wind-tunnel conditions for straight cones [21, 22]. It is proposed that non-modal perturbations growing upstream may be responsible for such a small transition *N*-factor.

Figure 19 depicts the logarithmic growth rate N_E of the optimal disturbance under three conditions as a function of spanwise wavenumber. The results have achieved grid and step-length independence. A systematic computation is carried out to obtain the optimal growth interval. For the flight condition, within the Cartesian coordinate system, the exit is selected at $X^* = 687$ mm, and the optimal interval ranges from $X^* = 566$ mm to 687 mm. For the wind-tunnel conditions, the exit is located uniformly at $X^* = 246$ mm. The optimal interval for the 2° AoA condition is from $X^* = 186$ mm to 246 mm, and for the 4° AoA condition, it is from $X^* = 197$ mm to 246 mm. It shows that the wave numbers of the optimal disturbances for the three conditions are relatively consistent, corresponding to a dimensional spanwise wavelength of roughly 5 mm. Based on the PSE3D-eN analysis results, the 2° AoA wind-tunnel condition reaches a *N*-factor of approximately 4 prior to the transition, which is greater than the optimal gain and thus might be dominated by the modal transition. By contrast,

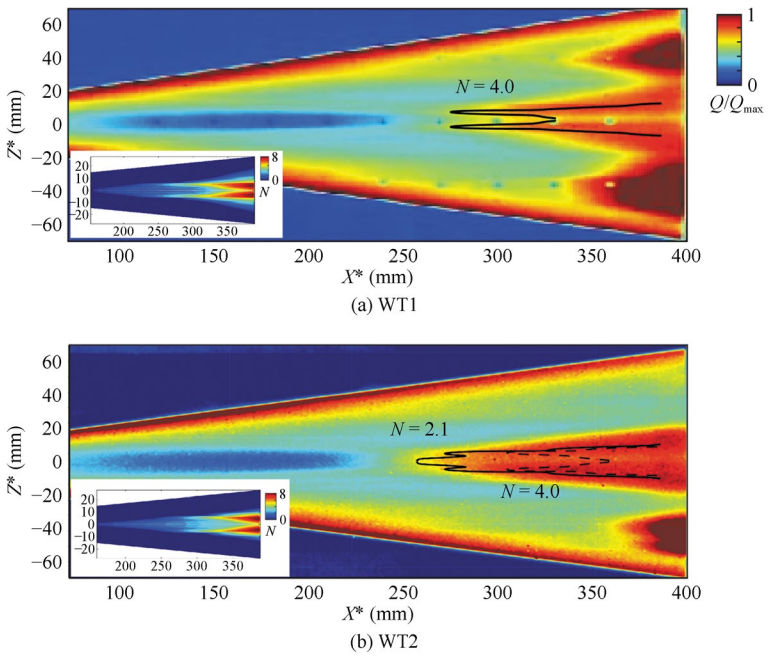

Fig. 18 Experimental results of temperature-sensitive paint under wind-tunnel conditions of cases **a** WT1 (2° AoA) and **b** WT2 (4° AoA) respectively, along with the transition *N*-factor front (solid and dashed lines) and the subplot standing for the *N*-factor distribution predicted by PSE3D

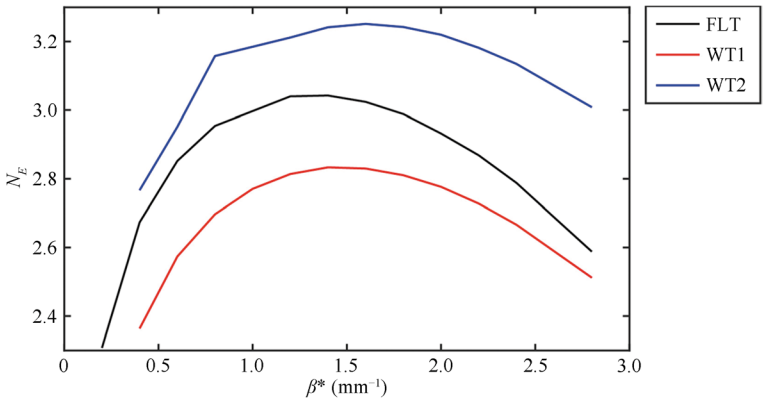

Fig. 19 The logarithmic amplification ratio N_E of the optimal disturbance as a function of wave number

the 4° AoA wind-tunnel condition reaches a N-factor of approximately 2 prior to the transition, which is smaller than the optimal gain ($N_E \approx 3.2$) and thus might be dominated by the non-modal transition.

4 Conclusions

The stability analysis of the windward surface of a lifting body at a flight condition and two wind-tunnel conditions is conducted and compared with the experimental and numerical results, focusing on the transition front prediction in this study. Under the flight condition, the global stability analysis reveals that the modal stability within the centerline region undergoes three distinct stages, namely, the initial stage dominated by Mack mode instabilities, followed by the second stage where inner modes prevail, and the third stage where outer modes take over owing to the strengthening of outer vortices. The most amplified mode at the transition location is the modulated oblique Mack mode at 110 kHz. The unstable modes of cross-flow disturbance are distributed within the frequency range of 0–40 kHz with the peak frequency residing at around 25 kHz. It should be noted that although the frequency distribution of cross-flow modes falls within the inner mode frequencies of streamwise vortices, the present study has not considered the possible interaction between these two kinds of instabilities. Further investigations are needed to throw light on whether such interactions will occur and, if so, the potential impact on N-factors. The transition fronts for both the vortex transition and cross-flow transition at a flight condition are successfully obtained by multi-dimensional stability analyses, while the conventional LST-eN method fails to capture the vortex transition front, but adequately obtains the cross-flow transition front with a larger transition N-factor than that from the PSE3D-eN method. This suggests that different N-factors may need to be selected as the transition criterion when employing different methods. The transition front in the vortex region is acquired via direct numerical simulation. A blowing-suction of 1% of the incoming flow velocity is employed upstream to facilitate transition. Based on the results, the magnitude of the blowing-suction is substantial enough to trigger transition prior to the instability of the vortex modes. The transition N-factor based on the direct numerical simulation is approximately 2.

The stability characteristics of the vortex region for the wind-tunnel cases closely resemble those observed under the flight condition, albeit with different flow

configurations. The dominant instability is the planar Mack mode upstream, followed by wide-band intrinsic vortex mode instability downstream, with a dominant frequency of approximately 92 kHz, slightly lower than the flight condition. The most significant disparity lies in the fact that planar Mack modes achieve the largest N-factor under wind-tunnel conditions, while oblique Mack modes dominate under the flight condition. Moreover, it is found that increasing the angle of attack stabilizes the vortex but simultaneously promotes the Mack mode. The heat flux data obtained from wind-tunnel experiments at different angles of attack reveal two distinct transition scenarios. One exhibits a dual front near the centerline, clearly indicating vortex transition, while the other shows only a single peak at the centerline. The vortex transition N-factor based on PSE3D for the former with a smaller AoA is approximately 4 according to the experimental transition position, whereas for the latter with a larger AoA it is only 2. Intriguingly, the higher AoA case experiences an earlier transition than the lower AoA case although the latter seems to be more unstable according to modal stability theories. An explanation to such a paradox is given based on the optimal growth analysis. It turns out that the optimal non-modal growth in the higher AoA case is significantly larger than that in the lower AoA case, thereby potentially inducing an earlier transition.

Abbreviations

DNS	Direct numerical simulation
PSE3D	Plane-marching parabolized stability equations
LST	One-dimensional stability theories
PSE3D-eN	Plane-marching parabolized stability equations based eN method
LST-eN	One-dimensional stability theories based eN method

Acknowledgements
The authors are thankful to Dr. Ao Wang at the State Key Laboratory of Aerodynamics for useful discussions.

Authors' contributions
Ligeng Zhang: Formal analysis; Investigation; Visualization; Writing - original draft; Writing - review and editing. Xi Chen: Investigation; Software; Writing - review and editing. Shuyi Liu: Data curation; Writing - review and editing. Qian Wang: Data curation; Writing - review and editing. Siwei Dong: Writing - review and editing. Maochang Duan: Data curation; Writing - review and editing. Jianqiang Chen: Funding acquisition; Resources; Supervision. All authors read and approved the final manuscript.

Funding
This work was supported by the National Natural Science Foundation of China (Grant No. 12372225).

Data availability
The datasets used and/or analysed during the current study are available from the corresponding author on reasonable request.

Declarations

Competing interests
The authors declare that they have no competing interests.

Received: 22 August 2024 Revised: 5 November 2024 Accepted: 22 December 2024
Published online: 27 June 2025

References

1. Chen J, Tu G, Zhang Y et al (2017) Hypersonic boundary layer transition: what we know, where shall we go. Acta Aerodyn Sin 35(3):311–337. https://doi.org/10.7638/kqdlxxb-2017.0030 (in Chinese)
2. Cebeci T, Shao JP, Chen HH et al (2004) The preferred approach for calculating transition by stability theory. In: Proceedings of the International Conference on Boundary and Interior Layers (BAIL 2004), Toulouse, 5-9 July 2004
3. Van Ingen JL (2008) The e^N method for transition prediction. Historical review of work at TU Delft. In: 38th Fluid Dynamics Conference and Exhibit, Seattle, 23-26 June 2008. https://doi.org/10.2514/6.2008-3830

4. Huang Z, Zhang Y (2023) Numerical research progress and prediction software of transition in hypersonic three-dimensional boundary layers. Acta Aerodyn Sin 41(11):1–19. https://doi.org/10.7638/kqdlxxb-2023.0014 (in Chinese)
5. Mack LM (1984) Boundary-layer linear stability theory. In: AGARD Special Course on Stability and Transition of Laminar Flow, Rhode-Saint-Genese 26-30 March 1984
6. Herbert T (1997) Parabolized stability equations. Annu Rev Fluid Mech 29:245–283. https://doi.org/10.1146/annurev.fluid.29.1.245
7. Alba CR, Johnson HB, Bartkowicz MD et al (2008) Boundary-layer stability calculations for the HIFiRE-1 transition experiment. J Spacecr Rockets 45(6):1125–1133. https://doi.org/10.2514/1.37445
8. Li F, Choudhari M, Chang CL et al (2012) Stability analysis for HIFiRE experiments. In: 42nd AIAA Fluid Dynamics Conference and Exhibit, New Orleans, 25-28 June 2012. https://doi.org/10.2514/6.2012-2961
9. Lakebrink MT, Paredes P, Borg MP (2017) Toward robust prediction of crossflow-wave instability in hypersonic boundary layers. Comput Fluids 144:1–9. https://doi.org/10.1016/j.compfluid.2016.11.016
10. Moyes AJ, Kocian TS, Mullen D et al (2018) Boundary-layer stability analysis of HIFiRE-5b flight geometry. J Spacecr Rockets 55(6):1341–1355. https://doi.org/10.2514/1.A34146
11. Tufts MW, Gosse RC, Kimmel RL (2018) Parabolized stability equation analysis of crossflow instability on HIFiRE-5b flight test. J Spacecr Rockets 55(6):1369–1378. https://doi.org/10.2514/1.A34149
12. Berridge DC, McKiernan GR, Wadhams TP et al (2018) Hypersonic ground tests in support of the boundary layer transition (BOLT) flight experiment. In: 2018 Fluid Dynamics Conference, Atlanta, 25-29 June 2018. https://doi.org/10.2514/6.2018-2893
13. Moyes AJ, Beyak ES, Kocian TS et al (2019) Accurate and efficient modeling of boundary-layer instabilities. In: AIAA Scitech 2019 Forum, San Diego, 7-11 January 2019. https://doi.org/10.2514/6.2019-1907
14. Moyes AJ, Reed HL (2021) Preflight boundary-layer stability analysis of BOLT geometry. J Spacecr Rockets 58(1):78–89. https://doi.org/10.2514/1.A34792
15. Kocian TS, Moyes AJ, Reed HL et al (2019) Hypersonic crossflow instability. J Spacecr Rockets 56(2):432–446. https://doi.org/10.2514/1.A34289
16. Song R, Zhao L, Huang Z (2020) Improvement of the parabolized stability equation to predict the linear evolution of disturbances in three-dimensional boundary layers based on ray tracing theory. Phys Rev Fluids 5(3):033901. https://doi.org/10.1103/PhysRevFluids.5.033901
17. Theofilis V (2011) Global linear instability. Annu Rev Fluid Mech 43:319–352. https://doi.org/10.1146/annurev-fluid-122109-160705
18. Paredes P, Gosse R, Theofilis V et al (2016) Linear modal instabilities of hypersonic flow over an elliptic cone. J Fluid Mech 804:442–466. https://doi.org/10.1017/jfm.2016.536
19. Chen X, Chen J, Dong S et al (2020) Stability analyses of leeward streamwise vortices for a hypersonic yawed cone at 6 degree angle of attack. Acta Aerodyn Sin 38(2):299–307. https://doi.org/10.7638/kqdlxxb-2020.0038 (in Chinese)
20. Li X, Chen J, Huang Z et al (2020) Stability analysis and transition prediction of streamwise vortices over a yawed cone at Mach 6. Phys Fluids 32(12):124110. https://doi.org/10.1063/5.0031057
21. Paredes P, Scholten A, Choudhari MM et al (2023) Modal instabilities over blunted cones at angle of attack in hypersonic flow. J Spacecr Rockets 60(4):1188–1200. https://doi.org/10.2514/1.A35590
22. Chen X, Tu G, Wan B et al (2024) The leeward vortex transition over hypersonic yawed cones by e^N method based on global stability theory. Acta Aerodyn Sin 42(1):33–44. https://doi.org/10.7638/kqdlxxb-2023.0055 (in Chinese)
23. Choudhari M, Li F, Paredes P (2020) Streak instabilities on HIFiRE-5 elliptic cone. In: AIAA Scitech 2020 Forum, Orlando, 6-10 January 2020. https://doi.org/10.2514/6.2020-0828
24. Choudhari M, Li F, Paredes P et al (2022) Evolution of high-frequency instabilities in the presence of azimuthally compact crossflow vortex pattern over a yawed cone. Theor Comput Fluid Dyn 36(2):181–204. https://doi.org/10.1007/s00162-021-00594-8
25. Butler C, McKiernan G, Wheaton BM (2023) Initial BiGlobal stability analysis of the BOLT II flight experiment. Paper presented at the AIAA SCITECH 2023 Forum, National Harbor, 23-27 January 2023. https://doi.org/10.2514/6.2023-0291
26. Araya D, Bitter N, Wheaton BM et al (2022) Assessment of linear methods for analysis of boundary layer instabilities on a finned cone at Mach 6. Paper presented at the AIAA AVIATION 2022 Forum, Chicago, 27 June - 1 July 2022. https://doi.org/10.2514/6.2022-3247
27. Araya DB, Bitter NP, Wheaton BM et al (2023) Linear analysis of boundary-layer instabilities on a finned-cone at Mach 6. arXiv preprint. arXiv:2303.10747
28. Liu S, Yuan X, Liu Z et al (2021) Design and transition characteristics of a standard model for hypersonic boundary layer transition research. Acta Mech Sin 37:1637–1647. https://doi.org/10.1007/s10409-021-01136-5
29. Tu G, Chen J, Yuan X et al (2022) Progress in flight tests of hypersonic boundary layer transition. Acta Mech Sin 37:1589–1609. https://doi.org/10.1007/s10409-021-01153-4
30. Liu S, Wang A, Duan M et al (2024) Characteristics of boundary layer stability of HyTRV model bottom. J Exp Fluid Mech, in press. https://doi.org/10.11729/syltlx20240014 (in Chinese)
31. Chen X, Dong S, Tu G et al (2022) Boundary layer transition and linear modal instabilities of hypersonic flow over a lifting body. J Fluid Mech 938:A8. https://doi.org/10.1017/jfm.2021.1125
32. Li X, Fu D, Ma Y (2008) Direct numerical simulation of hypersonic boundary layer transition over a blunt cone. AIAA J 46(11):2899–2913. https://doi.org/10.2514/1.37305
33. Chen J, Tu G, Wan B et al (2021) Characteristics of flow field and boundary-layer stability of HyTRV. Acta Aeronaut Astronaut Sin 42(6):124317. https://doi.org/10.7527/S1000-6893.2020.24317 (in Chinese)
34. Chen X, Dong S, Tu G et al (2023) Global stability analyses of Mack mode on the windward face of a hypersonic yawed cone. Phys Rev Fluids 8:033903. https://doi.org/10.1103/PhysRevFluids.8.033903
35. Reddy SC, Henningson DS (1993) Energy growth in viscous channel flows. J Fluid Mech 252:209–238. https://doi.org/10.1017/S0022112093003738
36. Paredes P, Choudhari MM, Li F et al (2016) Optimal growth in hypersonic boundary layers. AIAA J 54(10):3050–3061. https://doi.org/10.2514/1.J054912

37. Paredes P, Choudhari MM, Li F et al (2019) Nose-tip bluntness effects on transition at hypersonic speeds. J Spacecr Rockets 56(2):369–387. https://doi.org/10.2514/1.A34277
38. Chen X, Wan B, Tu G et al (2024) Non-modal growth analysis of high-speed flows over an inclined cone. arXiv preprint. arXiv:2406.18803v1
39. Andersson P, Brandt L, Bottaro A et al (2001) On the breakdown of boundary layer streaks. J Fluid Mech 428:29–60. https://doi.org/10.1017/s0022112000002421
40. Ren J, Fu S (2015) Secondary instabilities of Görtler vortices in high-speed boundary layer flows. J Fluid Mech 781:388–421. https://doi.org/10.1017/jfm.2015.490
41. Vaughan NJ, Zaki TA (2011) Stability of zero-pressure-gradient boundary layer distorted by unsteady Klebanoff streaks. J Fluid Mech 681:116–153. https://doi.org/10.1017/jfm.2011.177
42. Klebanoff PS (1971) Effect of free-stream turbulence on the laminar boundary layer. Bull Am Phys Soc 16:1323–1333
43. Chen X, Huang GL, Lee CB (2019) Hypersonic boundary layer transition on a concave wall: stationary Görtler vortices. J Fluid Mech 865:1–40. https://doi.org/10.1017/jfm.2019.24
44. Paredes P, Choudhari MM, Li F (2019) Instability wave-streak interactions in a high Mach number boundary layer at flight conditions. J Fluid Mech 858:474–499. https://doi.org/10.1017/jfm.2018.744
45. Chen X, Chen J, Yuan X et al (2019) From primary instabilities to secondary instabilities in Görtler vortex flows. Adv Aerodyn 1:19. https://doi.org/10.1186/s42774-019-0021-8
46. Zhang L, Dong S, Liu S et al (2022) Stability analysis of streamwise vortices over a blunt inclined cone under a hypersonic flight condition. Phys Fluids 34(7):074107. https://doi.org/10.1063/5.0099952
47. Haynes TS, Reed HL (2000) Simulation of swept-wing vortices using nonlinear parabolized stability equations. J Fluid Mech 405:325–349. https://doi.org/10.1017/S0022112099007260